

Durability Enhancement of Low Ice Adhesion Polymeric Coatings

Halar Memon, Davide S.A. De Focatiis, Kwing-So Choi and Xianghui Hou*

Faculty of Engineering, University of Nottingham, University Park, Nottingham NG7 2RD,
UK

*Correspondence: xianghui.hou@nottingham.ac.uk.

Abstract

Icephobic performance of low-ice adhesion polymeric coatings has been studied intensively for passive ice protection. However, limited efforts were conducted to identify strategies for enhancing the durability of the coatings to maintain low ice adhesion after erosion impact. In this work, we developed and investigated several polyurethane-based nanocomposite and fibre-reinforced coatings to understand the deteriorating behaviour of the coatings under rigorous impinging erosion tests and the subsequent impact on ice adhesion. The inclusion of fillers resulted in up to 38 points increase in Shore hardness relative to the pristine PU coatings. The ice adhesion strengths on 3 wt% nanoparticle-reinforced coatings after the erosion tests were nearly halved, whereas, a 5-fold reduction was observed on 3 wt% fibre-reinforced coatings compared to that of the pure PU coatings. Our results indicated that the incorporation of fillers was effective in reducing the ice anchoring points, and that, after the impingement, the icephobic performance was retained by either lowering surface roughness or by minimizing surface deterioration. Fibres took a more effective role in limiting crack initiation and resisting crack propagation. The ice adhesion strength of the coatings increased from 5.6 kPa to 8.4 kPa with 20 wt% carbon fibres incorporated PU coatings, essentially keeping the adhesion below 10 kPa even after rigorous impinging tests and a ~10-fold reduction in ice adhesion strength as compared to the pure PU coatings. The incorporation of

24 the fibres led to enhanced durability and retention of excellent icephobic performance via a
25 mechanism that is adaptable to other polymeric coatings.

26 Keywords: Carbon fibres, ice anchoring, durability, icephobicity, polyurethane

27 **1 Introduction**

28 Polymeric surfaces and coatings have been a popular choice for passive ice protection and
29 many reports have indicated low ice adhesion strength on polymeric coatings and surfaces [1-
30 4]. Polydimethylsiloxane (PDMS) and polyurethane (PU) are the major candidates in the
31 development of icephobic coatings, and their icephobic performance has been studied
32 intensively [5-7]. However, limited efforts have been paid on the durability of the coatings
33 and their capability to maintain icephobic performance after erosion impact. Most studies
34 have either conducted icing/de-icing cycles [8-11], chemical stability [12-14], and/or
35 durability evaluation using mechanical methods (such as abrasion resistance, indentations,
36 scratch tests, and sandblasting etc.) [14-18]. Wu et al. [19] tested their sol-gel coatings by
37 nanoindentation, pencil-scratch resistance, and weight loss rate under different sandblasting
38 conditions, indicating that the measured ice adhesion strength was maintained below 70 kPa
39 after mechanically endured durability tests. Beemar et al. [20] reported an ice adhesion
40 strength at around 6 kPa, even after 1000 abrasion cycles on a PDMS gel surface. Zhuo et al.
41 [21] measured an increase in ice adhesion strength from 12 kPa to 20 kPa after 800 abrasion
42 cycles on a PDMS coating. Liu et al. [22] carried out an impinging study on a PDMS
43 nanocomposite coating using a silicon carbide suspension at 37 m/s velocity and a liquid flow
44 rate of 72 mL/min, but did not re-evaluate the ice adhesion strength after the impinging
45 erosion.

46 The research interest to explore the inclusion of hard materials in a soft polymer matrix is
47 overwhelming, and many studies have been conducted to investigate the mechanical
48 properties of composites reinforced with fibrous and/or nano inclusions [14-18]. The key
49 application areas of icephobic coatings are in aerospace and wind energy, both of which
50 involve rigorous water droplet erosion. A leading edge of aircraft often suffers ice crystals
51 impingement in sub-zero temperatures and/or rain droplets erosion. Wind turbine blades may

52 undergo severe water droplet impingement as well and coating erosion resistance under the
53 working conditions is also critical. Therefore, the designed icephobic coatings need to resist
54 such surface erosion damage (morphological and/or topographical) that may deteriorate the
55 icephobic performance.

56 In this study, polyurethane (PU) based low ice adhesion coatings were formulated and
57 reinforced with nanoparticles and micro-fibres. The main aim of this study was to explore an
58 effective approach to enhance the durability of the icephobic coatings. The incorporation of
59 micro-fibres and nanoparticles in this work was driven by the need to enhance durability in
60 surface icephobicity under erosion impact, even after non-ignorable material damage. Water
61 impinging tests using silicon carbide (SiC) particle suspension were used to simulate the
62 water droplet erosion. It was suggested that the inclusion of fibres was more beneficial in this
63 context than the nanoparticles. The addition of fibres helps to distribute the droplet impact
64 energy more widely across the polyurethane matrix and helps to reduce the stress
65 concentration points on the coating surface by minimizing crack initiation during the
66 incubation period. Thus, less ice anchoring on the surface would be formed, leading to easier
67 ice removal and maintaining the desirable icephobic performance even after the erosion
68 impacts.

69 **2 Experiments**

70 Four types of polyurethane coatings were formulated in this study, and each coating was
71 characterised and compared in terms of surface roughness, morphology, and ice adhesion
72 strength before and after the impingement test.

73 **2.1 Substrates and raw materials**

74 Aluminium 2024-T4 plates with a size of 50 mm x 20 mm x 1 mm were used as substrates. A
75 two-part thermoset polyurethane resin, PMC-790 (PU), was purchased from Smooth-on

76 (USA). Kevlar Aramid pulp, Twaron ® 5011 (Kevlar fibres, 125 µm average length), was
 77 kindly provided by Teijin Aramid GmbH (Germany). Carbisol Mil 100µ (milled carbon
 78 fibres, 80-100 µm average length) was obtained from easycomposites (UK). Reduced
 79 graphene nanoplatelets, CamGraph G3 (GR, lateral size of ~400 nm and flake thickness of ~3
 80 nm), were purchased from FGV Cambridge Nanosystems (UK). Nanodiamonds powder (ND,
 81 spherical size ≤100 nm) was procured from Jichang Metal processing Ltd. (China). Silicon
 82 carbide particles (SC224 600 mesh) for the water impinging erosion test were supplied by
 83 Simba Materials (UK). Triton X-100 was purchased from Sigma-Aldrich (UK). All materials
 84 were used as received.

85 2.2 Preparation of coatings

86 All aluminium plates were sandblasted to enhance the coating adhesion, using a Guyson
 87 F1200 sandblaster with 180-220 µm alumina particles. The substrates were then washed with
 88 ethanol and deionized water thrice and dried using compressed air before the coating
 89 application.

90 PU solutions were magnetically stirred at a Part A : Part B ratio of 2 : 1 by weight as listed in
 91 table 1. Different fillers were introduced and mixed in the resin solution during the stirring,
 92 The PU resins were then ultrasonically mixed for a further 30 minutes, and brush coated on
 93 the sandblasted aluminium substrates. All PU coatings with and without fillers were cured at
 94 25 °C for 48 hours and post-treated at 65 °C for 4 hours.

95 Table 1: List of sample types and their compositions

Sample types	Sample codes	Coating type	Filler content (wt%)
Pure PU coatings (PU)	PU	Pristine	-
PU coatings with carbon fibres (PU-CF)	PU-CF-0.5	Fibre-reinforced	0.5
	PU-CF-1		1

	PU-CF-3		3
	PU-CF-5		5
	PU-CF-20		20
PU coatings with Kevlar fibres (PU-KV)	PU-KV-0.5	Fibre-reinforced	0.5
	PU-KV-1		1
	PU-KV-3		3
	PU-KV-5		5
	PU-KV-20		20
PU coatings with nanodiamond (PU-ND)	PU-ND-0.5	Nanocomposite	0.5
	PU-ND-1		1
	PU-ND-3		3
	PU-ND-5		5
	PU-ND-20		20
	PU-ND-40		40
PU coatings with graphene (PU-GR)	PU-GR-0.5	Nanocomposite	0.5
	PU-GR-1		1
	PU-GR-3		3
	PU-GR-5		5

96

97 **2.3 Surface characterization**

98 A Zeta-20 non-contact optical profiler was used to evaluate the surface roughness. The
99 roughness values reported were the average of a minimum of 30 measurements, and R_a was
100 measured over a line stretching across the observed surface. The same system was used to
101 observe topographical changes on the surfaces after erosion. An FEI Quanta 650 ESEM
102 (environmental scanning electron microscope) was used to acquire microstructural images
103 and morphological changes on the eroded coatings.

104 Shore hardness was measured using a SAUTER durometer having Shore hardness A and D
105 scales. The durometer was attached to SAUTER test stands TI-AO and TI-D for Shore
106 hardness A and D scales, respectively. The hardness reported was an average penetration
107 (Shore) value based on 10 separate measurement. Supplementary table 1 outlines the
108 complete data of surface roughness and Shore hardness measurements.

109 **2.4 Evaluation of hydrophobicity and icephobicity**

110 The sessile drop technique was used to measure water contact angles (WCAs) using an
111 FTÅ200 goniometer and 5 µl water drops were used. The tests were conducted at room
112 temperature, and further details of the measurement were described in our previous work [23,
113 24].

114 A MOOG G403-2053A servo motor was used to measure the ice adhesion strength tests via a
115 centrifugal method and the test was performed in an environmental chamber (ALPHA 1550-
116 40H) to simulate the freezing conditions. The ice adhesion test was conducted at a
117 temperature of -10 °C and the testing method was described previously [23, 24]. The ice
118 formation and ice adhesion test were conducted at -10 °C and are depicted in figure 1. The
119 bulk ice formation was carried out using a silicon mould attached on the coating surface, as
120 shown in figure 1a. The samples were then spun in the centrifugal chamber with a
121 counterweight (figure 1b) and the speed at the time of ice detachment was obtained.

122 The centrifugal shearing force F (N) is determined from Eq. (1):

$$123 \quad F = mr\omega^2 \quad (1)$$

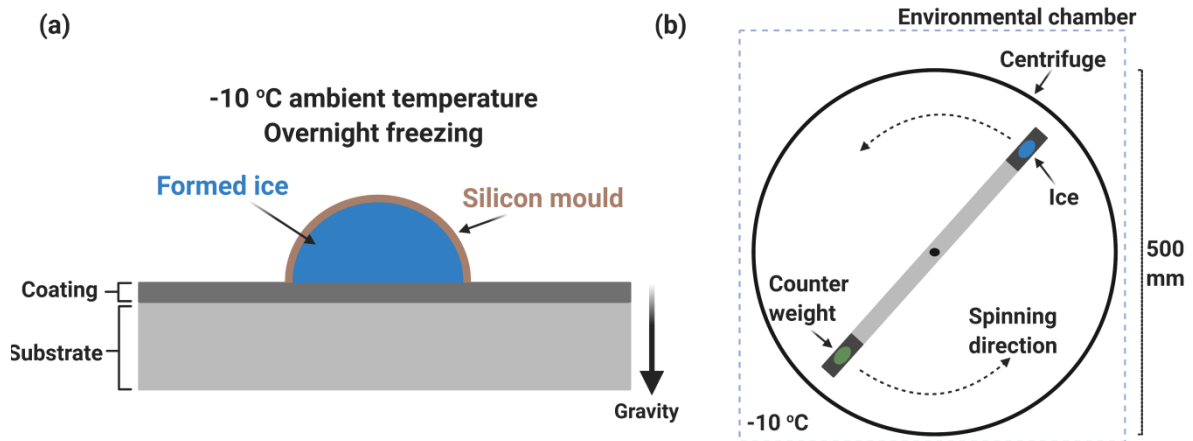
124 where ω (rad/s) is the rotational speed at the point of ice removal, r (m) is the rotor length,
125 and m (kg) is the mass of ice. The ice (shear) adhesion strength τ_{ice} can then be calculated as

$$126 \quad \tau_{ice} = F/A \quad (2)$$

127 where A (m²) is the substrate/ice contact area.

128 The centrifugal method to evaluate the ice adhesion strength in this work had been previously
129 applied by many researchers [25-27] and a recent comparative study indicated its
130 compatibility with the other widely used methods such as horizontal force transducer method
131 [28]. However, the values of ice adhesion strength using different evaluation approaches
132 could not be directly compared at this moment, due to the variations of ice formation

133 conditions, testing setup and testing parameters, etc. The ice adhesion strength measured
134 using centrifugal methods tends to be lower as compared to that of vertical/horizontal push
135 methods. The static and dynamic water contact angles (WCAs), including advancing WCAs
136 (AWCAs), receding WCAs (RWCAs), contact angle hysteresis (CAH), and ice adhesion
137 strength measurement are summarized in supplementary table 1.



138

139 Figure 1: (a) Ice formation on a sample surface and (b) the details of the centrifugal testing
140 method (figure created using biorender.com)

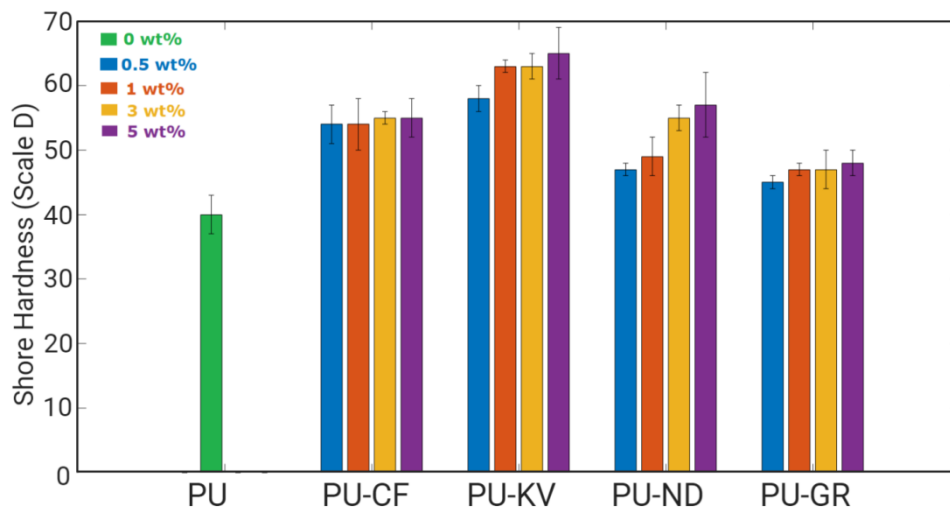
141 2.5 Water impinging erosion tests (WIETs)

142 To evaluate the coating durability, erosion tests from the impingement of silicon carbide
143 aqueous suspension were carried out. The silicon carbide suspension was prepared using 1
144 wt% silicon carbide microparticles and 0.1 wt% of Triton X-100. The suspension was then
145 magnetically stirred for 4 hours. During the impinging test, the suspension was pressurized
146 through a PNR ultrasonic atomiser nozzle (MAD 0331 B1BB) using compressed gas and the
147 micro-droplets impinged onto the coating specimen. The system was maintained at a liquid
148 flow rate of 1.2 mL/s, a distance between the nozzle and the specimen of 4 cm, and a duration
149 of 90 minutes. The method had been described in detail elsewhere [22]. The surface
150 morphology, surface roughness and ice adhesion strength of the coatings were measured
151 before and after the erosion tests.

152 **3 Results and discussion**

153 **3.1 Effect of incorporated fillers on coating hardness**

154 The pure PU coatings exhibited a Shore hardness of 40D, and the incorporation of fillers
155 increased the hardness, especially for PU-KV-5, where 24 points increase was observed to
156 64D. The incorporation of fillers in PU-GR and PU-CF coatings led to an enhancement of the
157 hardness. However, the increase in hardness was relatively insensitive to the amount of filler
158 as shown in figure 2. In the PU-KV and PU-ND coatings, a significant increase in the
159 hardness was observed with increasing filler content. Generally, the inclusion of fillers
160 increased the hardness of the polymeric coatings by 12~62%. Shore hardness values could be
161 used as representative values for elastic modulus [29] and the representative values are
162 equivalent to elastic modulus measured via other typical methods [30].



163

164 Figure 2: Effect of fillers on the Shore D hardness of polymer coatings

165 **3.2 Microstructural observation of the polymeric coatings**

166 The influential role of surface roughness on ice adhesion strength is mainly due to the ice
167 anchoring process on the surface [23, 24]. As the material suffers erosion attack, the surface
168 morphology is randomly deteriorated in a way that could influence the icephobic
169 performance of the coatings. The impinged surface may generate some ice anchoring points

170 which would increase ice adhesion strength due to mechanical interlocking of the ice on the
171 surface. Changes in the surface roughness on all the coatings as a result of the impingement
172 were also measured and listed in supplementary table 1.

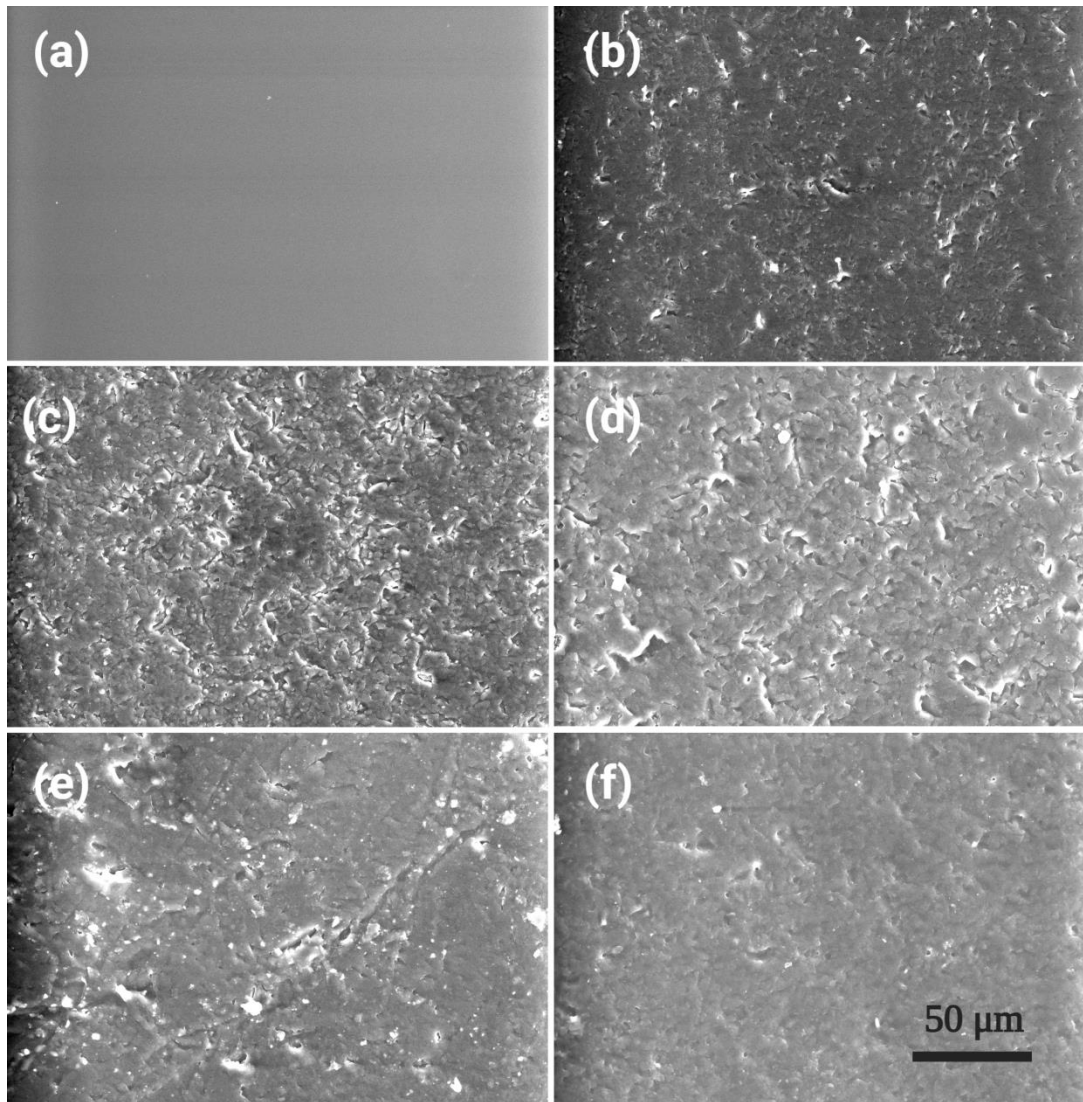
173 **3.2.1 PU coatings**

174 The microstructural images of the pristine PU coatings and their surface after WIETs are
175 shown in figure 3. It is evident that the surface morphology had been significantly altered and
176 the surface was much rougher after WIETs. The impinging water droplets and SiC particles
177 created cavities on the surface as shown in figure 3b. The surface roughness (R_a) also
178 drastically increased from $0.08\ \mu\text{m}$ to $0.45\ \mu\text{m}$ on the PU coatings after WIETs. The pure PU
179 coating was also studied over a larger area and the 3D profile of an impinged PU coating is
180 shown in supplementary figure 1a. The figure shows a valley where the cavities are $\sim 25\text{-}80$
181 μm deep, making them easy to induce mechanical interlocking of ice. The initial water
182 condensation and subsequent ice formation had been observed in the surface cavities in our
183 previous work [23, 24].

184 **3.2.1.1 Polymeric nanocomposite coatings**

185 The surface morphology of PU-ND-3 coatings (figure 3c), has also changed considerably
186 after WIETs. The surface morphology of PU-GR-3 compared with PU-ND-3 coatings after
187 WIETs are provided in supplementary figure 2a and 2b. The PU-GR-3 and PU-ND-3
188 coatings had surface roughnesses (R_a) of $0.1\ \mu\text{m}$ and $0.07\ \mu\text{m}$ respectively before WIETs,
189 and a clear increase in surface roughness to $0.21\ \mu\text{m}$ was observed on both nanocomposite
190 coatings after WIETs. Notably, the change in surface roughness was much lower than that
191 observed on the pure PU coatings, indicating that the incorporation of fillers resisted the
192 erosion attack on the nanocomposite surfaces. A mixture of cracks and cavities were formed
193 after WIETs on the surface of PU-ND-3 coating (figure 3c), instead of the cavities observed

194 on the pure PU coatings in figure 3b. 3D surface profiles of PU-ND-3 and PU-GR-3 are
195 given in supplementary figure 1b and 1c, respectively. The depth of cavities is considerably
196 reduced on both nanocomposite coatings as compared to the pure PU coatings, and the
197 cavities are up to 25 μm deep.



198

199 Figure 3: Microstructural images of (a) before and (b) after WIETs on the pure PU coatings
200 and after WIETs on (c) PU-ND-3, (b) PU-ND-20, (e) PU-KV-3, and (f) PU-KV-20 coatings

201 3.2.1.2 Polymeric fibre-reinforced coatings

202 The microstructural image of PU-KV-3 coatings after WIETs is shown in figure 3e. Similar
203 images after WIETs on PU-CF-3 compared with PU-KV-3 coatings are given in

204 supplementary figure 2c and 2d, respectively. Surface roughness (R_a) changed from 0.07 μm
205 on PU-CF-3 coatings to 0.27 μm and from 0.10 μm on PU-KV-3 coatings to 0.25 μm after
206 WIETs. Both impinged fibre-reinforced coatings indicated a larger increase in surface
207 roughness as compared to the impinged nanocomposite coatings. Closer inspection of figure
208 3e and supplementary figure 2c suggests that a significant portion of polymeric surface was
209 largely intact and the fibres were effective to restrain crack initiation, significantly reducing
210 the number of surface cavities.

211 The material damage around the fibres in the composite coatings is shown in figure 5c and
212 5d. 3D profile of impinged PU-KV-3 surface, shown in supplementary figure 1d, indicates
213 the surface damage incurred after the erosion tests. The 3D profile of impinged PU-CF-3
214 coatings is shown in supplementary figure 1e. The cavities on both fibrous coatings are ~40-
215 70 μm in depth.

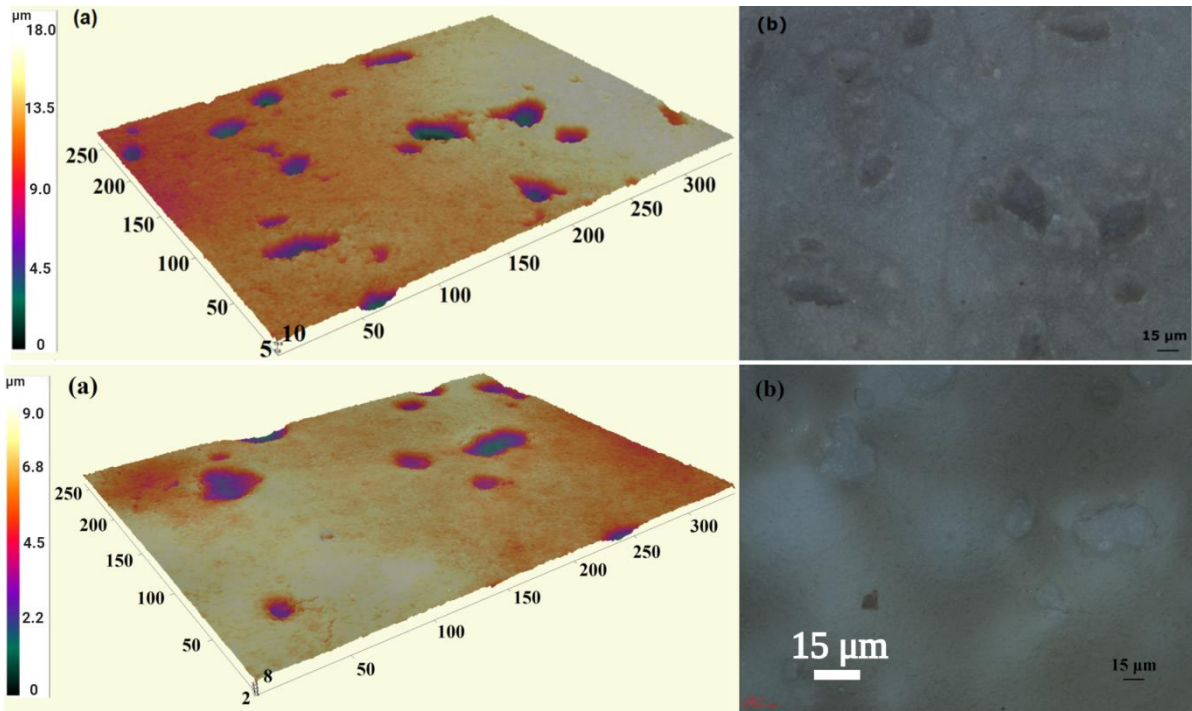
216 **3.2.2 Inclusion of high weight percentages of fillers**

217 In section 3.2.1, the coatings incorporated with 3 wt% fibres demonstrated more promising
218 results in terms of maintaining icephobic performance than the equivalent loading of
219 nanoparticles. In this section, coatings with higher filler contents were prepared to explore the
220 possibility of enhancing the durability of the polyurethane matrix. This could further reduce
221 the number of ice anchoring points and help to maintain low ice adhesion strength.

222 **3.2.2.1 PU nanocomposite coatings**

223 The incorporation of nanodiamonds in PU coatings was limited to a maximum of 40 wt%.
224 Further incorporation was difficult to process as the formulated solutions were highly
225 viscous, thus, not suitable for the brush application. The surface roughness (R_a) changed from
226 0.21 μm to $0.24 \pm 0.03 \mu\text{m}$ (slight increase) on PU-ND-20 and from 0.21 μm to 0.17 ± 0.02
227 μm (slight decrease) on PU-ND-40 before and after WIETs. Overall, the surface roughness

228 after WIETs decreased with a higher concentration of nanodiamonds. The surface
229 morphology of PU-ND-40 coating after WIETs and the surface cavities generated are shown
230 in figure 4a and 4b, and the cavities have the depth around 13 μm , whereas those on PU-ND-
231 3 surface are $\sim 25 \mu\text{m}$ deep (supplementary figure 1b).

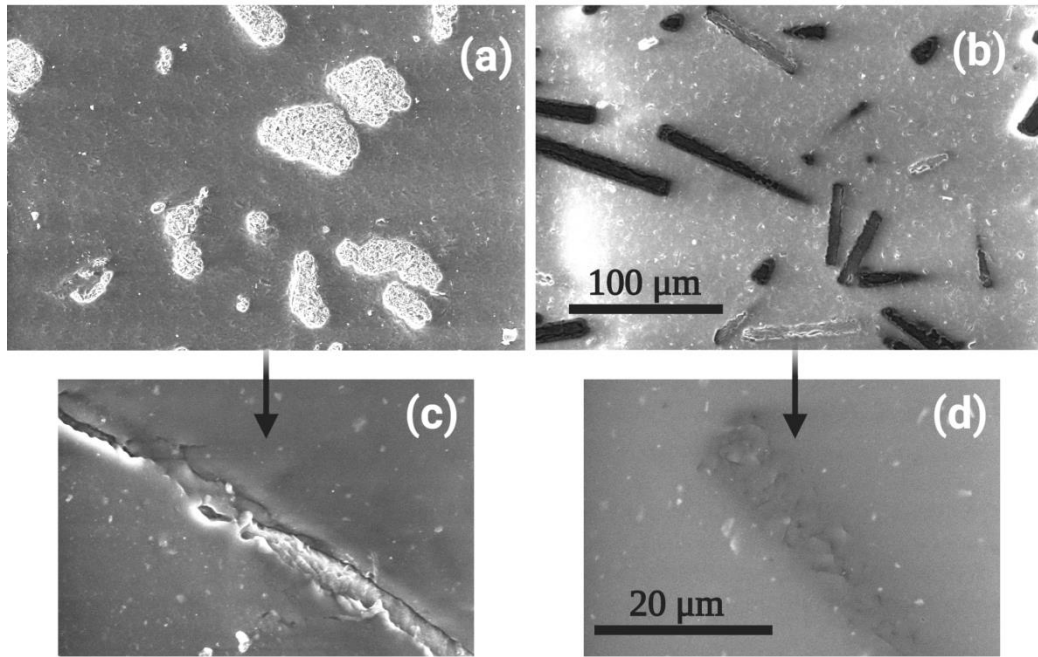


232
233 Figure 4: (a) 3D profile and (b) 2D image of PU-ND-40 coatings and (c) 3D profile and (d)
234 2D image of PU-KV-20 coatings after WIETs

235 The morphological changes on PU-ND-3 and PU-ND-20 surfaces are shown in figure 3c and
236 3d, respectively. It is clear that the morphological damage on the surface was further reduced
237 with a higher concentration of nanodiamonds and the number of cavities was considerably
238 reduced. Figure 3d indicates that the cavities on PU-ND-20 surface, which could be ice
239 anchoring sites, were reduced in both the numbers and the depth when compared to those on
240 PU-ND-3 coatings, as shown in figure 3c.

241 3.2.2.2 Fibrous PU coatings

242 A maximum of 20 wt% of Kevlar and carbon fibres were incorporated in the PU matrix, and
243 the microstructural images of both fibre-reinforced coatings after the erosion damage are
244 shown in figure 4b and supplementary figure 3. Both coatings demonstrated promising
245 durability during WIETs and the surface roughness did not change significantly compared to
246 that on as-prepared surfaces. The surface roughness (R_a) on PU-CF-20 coatings changed from
247 0.12 μm to 0.15 μm after WIETs, and from 0.12 μm to 0.22 μm on PU-KV-20 coatings. The
248 20 wt% fibre-reinforced coatings demonstrated the lowest increase in surface roughness after
249 WIETs across all the studied coatings. The depth of cavities on PU-KV-20 coatings was in
250 the range of $\sim 2\text{-}7 \mu\text{m}$, nearly halved in magnitude compared to those on PU-ND-40 coatings.
251 The number of cavities was also reduced on the 20 wt% fibre-reinforced coatings as
252 compared to those on the 3 wt% fibre-reinforced coatings. A comparison between PU-KV-3
253 and PU-KV-20 coatings is shown in figure 3e and 3f. The high filling of fibres in
254 polyurethane coatings was in favour of resisting the microstructural damage caused by the
255 erosion. Less number of surface cavities was observed on the 20 wt% fibre-reinforced
256 coatings, and the depth of the cavities was also reduced. In terms of fibres, carbon fibres in
257 this study were more effective in resisting the morphological changes when compared to
258 Kevlar fibres, as shown in figure 5a and 5b. Figure 5 also indicates an obvious size reduction
259 of the cavities on PU-CF-20 coatings and the size of cavities is significantly reduced (around
260 10 μm).



261

262 Figure 5: (a) PU-KV-20 and (b) PU-CF-20 coatings after WIETs. Possible material damage
 263 around the incorporated (c) Kevlar and (d) carbon fibres

264 **3.2.3 Impact of impinging erosion on ice adhesion strength**

265 Many researchers have used cyclic de-icing tests to evaluate icephobic performance of the
 266 coatings [8-11] and abrasion tests to evaluate the durability icephobic coatings [14-18].
 267 However, the impingement test is more representative of real-application conditions to
 268 evaluate the coating durability when considering the potential applications in aerospace and
 269 wind turbine. Ice adhesion strengths, before and after WIETs, on specific coatings are shown
 270 in figure 6d. Generally, the coating hardness had a direct effect on ice adhesion strength.

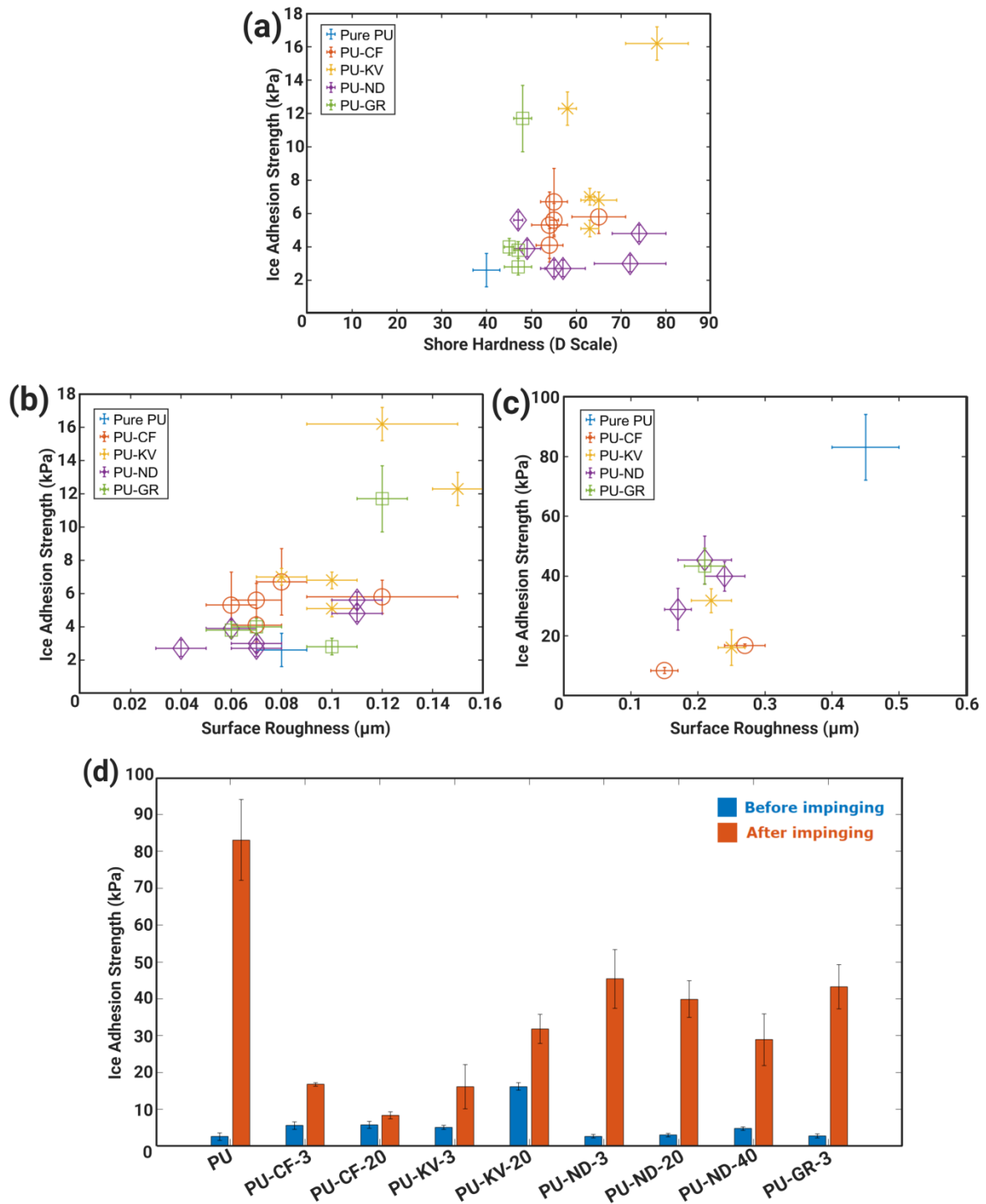
271 **3.2.3.1 Pre-impingement tests**

272 Ice adhesion strengths on all the as-prepared samples were less than 7 KPa, except for PU-
 273 KV-0.5, PU-KV-20, and PU-GR-5 coatings, as indicated in figure 6b. Higher ice adhesion
 274 strengths on PU-KV-20 and PU-GR-5 are thought to be due to the changes in morphology
 275 resulted from the higher filler concentrations. PU-KV-0.5 is an exception and its relatively

276 high ice adhesion strength may be mainly attributed to surface defects formed during the
277 coating preparation, which is evidenced by the higher surface roughness as listed in
278 supplementary table 1. A direct relation of ice adhesion strength with shore hardness is drawn
279 in figure 6a. For example, the incorporation of 20 wt% of Kevlar fibres in the PU matrix
280 leads to an increase in shore hardness to 78D and a 4-fold in ice adhesion strength was
281 measured. The incorporation of fillers could alter the surface characteristics and influence the
282 ice formation process, as observed in the PU-KV-0.5 coatings. Generally, the ice adhesion
283 strength increased with the incorporation of fillers, but they were mostly kept under 10 kPa
284 before WIETs.

285 **3.2.3.2 Post-impingement tests**

286 The ice adhesion of the pristine and impinged PU coatings is 2.6 kPa and 83.1 kPa
287 respectively, indicating approximately 32-fold increase after the erosion. Compared to the
288 values of the pure PU coatings, the ice adhesion strength of PU-GR-3 coatings after WIETs
289 was nearly halved. Similar results were also observed on PU-ND-3 coatings for which the ice
290 adhesion strength changed from 2.7 kPa to 45.4 kPa after WIETs. This value of PU-KV-3
291 coatings changed from 5.1 kPa to 16.1 kPa after WIETs; while on PU-CF-3, it increased from
292 5.6 kPa to 16.8 kPa. Overall, the ice adhesion increased by approximate 3 folds on the 3wt%
293 fibrous PU coatings after WIETs. The incorporation of high filling of nanodiamonds (higher
294 than 3 wt%) resulted in reduced ice adhesion as compared to that of PU-ND-3 coatings. The
295 ice adhesion strength on PU-ND-20 coatings decreased from 39.9 kPa to 28.9 kPa on PU-
296 ND-40 coatings. The increase in ice adhesion on PU-KV-20 and PU-CF-20 coatings after
297 WIETs was 1.4 fold and 2-fold, respectively. Compared to the pure PU coatings, a ~10-fold
298 reduction in ice adhesion strength after WIETs was obtained on the PU-CF-20 coatings,
299 whereas it was a ~5-fold reduction on the PU-KV-20 coatings.



300

301

302

303

304

305

Figure 6: Ice adhesion strength in comparison to (a) Shore D hardness values, surface roughness (b) before and (c) after WIETs. (d) Ice adhesion strength before and after WIETs. The incorporation of fillers was effective in resisting the formation of larger and/or deeper cavities, as shown in figure 3, and the possible ice anchoring was either reduced or weakened. These specific changes in ice adhesion strength indicate that the post-impingement icephobic

306 performance was intrinsically dependent on the filler contents and structures. Fibres are likely
307 to induce less ice anchoring points and fewer microstructural changes after WIETs. The
308 ability of ice to anchor on the surface is highly reliant on the surface roughness [23, 24], and
309 the post-impingement ice adhesion is plotted against the impinged surface roughness in figure
310 6c. It is evident that the fibre-reinforced surfaces minimized the surface crack propagation
311 and there were fewer anchoring points available, thus facilitating the removal of ice. The
312 figure also highlights the dominating role of surface roughness and no apparent correlation
313 with the relation to shore hardness values is observed. Fundamentally, the inclusion of fillers
314 results in improved durability of the PU coatings. In terms of icephobic performance, it is
315 impressive that PU-CF-20 coatings still maintains the ice adhesion strength below 10 kPa
316 after the silicon carbide suspension impinging erosion, and only a 1.4 fold increase in ice
317 adhesion strength is observed, which is a significant improvement as compared to that on the
318 pure PU coatings.

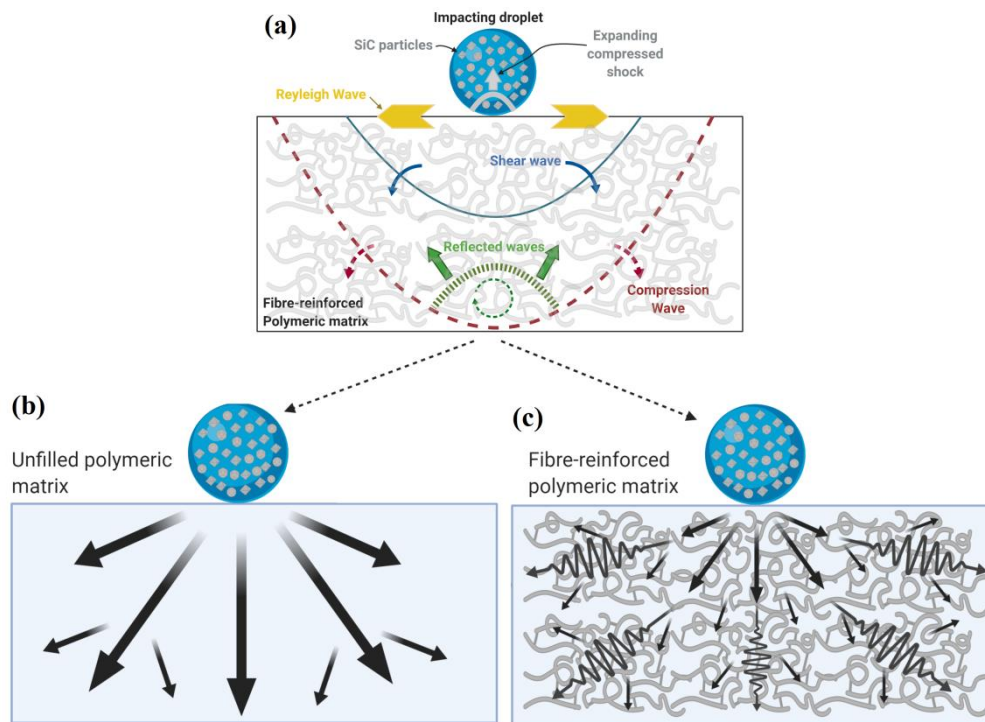
319 **3.3 Surface durability enhancement mechanisms**

320 The enhanced durability on the polymeric coatings could be explained in two distant
321 mechanisms: surface characteristics and erosion resistance. Firstly, polymeric coatings with
322 low elastic modulus are likely to induce low ice adhesion strength. It was reported that ice
323 adhesion strength decreased with the decrease of polymeric cross-link density [13, 31]. From
324 literature, the incorporation of Kevlar fibres, carbon fibres, nanodiamonds [32-34], and
325 graphene [35] often indicated a significant increase in mechanical properties of the polymeric
326 matrix. The Shore hardness measured in this work also indicates the enhanced hardness after
327 the incorporation of fillers, which also suggests an increase in the elastic modulus [29]. Thus,
328 the results support the need to lower down elastic modulus of polymers to induce a low ice
329 adhesion. However, ice shear mechanism is a complex phenomenon and requires similar
330 surface characteristics to draw conclusions. The surface roughness of the coatings is a

331 dominating factor for the ice adhesion strength [24]. Surface anomalies or cavities play an
332 important role and could encourage ice anchoring that may enhance ice adhesion strength.
333 The incorporation of carbon and Kevlar fibres produced mechanically reinforced composite
334 coatings. However, at 20 wt% fibres loading, the Kevlar-reinforced coatings suffered higher
335 damage, evidenced by the deeper and wider cavities as compared to those on carbon fibres
336 reinforced coatings. The damage on PU-KV-20 coatings could be explained from the fibre
337 interface bonding and the fibre aspect ratio. Firstly, In terms of fibre interfacial bonding with
338 the polymeric matrix, carbon fibres demonstrated higher interfacial strength than Kevlar
339 fibres, as reflected from the eroded coating surface: the carbon fibre was still tightly packed
340 in the polyurethane matrix, whereas the Kevlar fibre was exposed after the erosion impact
341 (figure 5c and 5d). Secondly, the interfacial bonding of fibres is closely related to the
342 toughening mechanisms, such as fracture energy and fracture toughness, and the work of
343 fracture would be greatly increased due to interfacial friction between the matrix and fibres
344 [36]. Lastly, the mechanical properties were demonstrated to be strongly dependent on the
345 aspect ratio of the reinforcing fibres, and the aspect ratio of the carbon fibres (~14) used in
346 this work is much higher than that of Kevlar fibres (~3). It is believed that filler with a higher
347 aspect ratio would provide greater resistance against erosion impact [37].

348 Secondly, the erosion of material induces cracks on the surface. The crack initiation and
349 propagation can be described as a combination of four mechanisms: (1) direct removal of
350 material or deformation caused by the direct high-speed impact; (2) propagation of stress
351 waves across the material; (3) fatigue incurred by the surface with repetitive droplet
352 impinging; (4) the inability of material to elastically recover (progression into plastic
353 deformation region) before the next impact event [38]. The erosion resistance depends on
354 how the material behaves at the impact zone and how stress waves generated at the impact
355 zone are propagated to the rest of the solid target. These stress waves consist of three

356 multidirectional waves as illustrated in figure 7a [39]. The velocities at which these waves
 357 propagate depend on the material density, Poisson's ratio and elastic modulus of the target.
 358 Microstructural discontinuities also result in enhanced stress waves due to stress
 359 concentrations on the surface, and the material may experience structural failure if the stress
 360 waves exceed the dynamic fracture strength of the target material [40].



361
 362 Figure 7: (a) Stress waves generated after the impact of a water droplet/sand particles (The
 363 mechanism is adapted from [39]) and the stress waves on (b) a pristine polymer and (c) a
 364 fibre-reinforced polymer (figure created using biorender.com)

365 Erosion resistance of the polyurethane coatings, thus, could be imparted by carefully
 366 selecting and incorporating fillers in the matrix in order to distribute the stress waves
 367 effectively. However, it is imperative to understand the causes that initiate the erosion
 368 deterioration in the coatings and which material properties could be linked to erosion
 369 initiation. Erosion initiation in wind turbine blades has been widely debated and surface
 370 fatigue was identified as a key failure mechanism [41-43]. Fatigue of the coating during
 371 erosion can be explained using two mechanisms. Firstly, water impinging is a form of

372 repetitive loading and the fractures are often observed after the spot has been struck by
373 several impacts [44]. In this work, the impingement test consists of a mixture of water with
374 hard SiC particles, and the particles could inflict a higher scratch and cause more damage
375 upon impact as compared to water droplets, as illustrated in figure 7b. The depletion and
376 deterioration of the surfaces caused by impinging particles were also observed in figure 3, 4,
377 and 5. Secondly, the fractures caused by the erosion may lead to a fatigue failure [45].
378 However, Alder et al. [46] indicated that fatigue may play a secondary role. They found that
379 the topological changes in the surface or cracks initiations during the incubation period are
380 the main factors that accelerate the erosion rate. Thus, erosion resistance could be imparted in
381 the polymeric coatings by deploying materials and/or incorporation of fillers that limits crack
382 initiation and propagation, and preventing the generation of stress concentration points which
383 may accelerates the erosion rate [47]. These cracks may also prompt the possible formation
384 of ice anchoring points, resulting in the mechanical interlocking of ice on the surface. Thus,
385 preventing the crack initiations on the surfaces has clear advantages for maintaining
386 icephobic performance.

387 High erosion resistance in elastomers is linked to their viscoelastic behaviour and low
388 modulus prevents the pressure buildup, thus avoiding the stress concentrations across the
389 surface, making them a better candidate for heavy rain impact erosions [44]. However,
390 elastomers frequently fail underneath the surface under repetitive loads, while the surface
391 remains intact. The erosion process on the fibre-reinforced elastomeric coatings could be
392 explained by two modes. Firstly, the local resin removal may result in the exposure of fibres
393 to the erosive environment. Secondly, there could be breakage of fibres as a result of direct
394 impingement and cracks may start to form around and perpendicular to the fibre length as
395 shown in figures 5c and 5d. Erosion impact on unfilled thermoset polymers induces breakage
396 and massive chunking of resin due to their brittle behaviour. A massive increase in surface

397 roughness was observed on the unfilled PU coatings in this study, as illustrated in figure 3b
398 and supplementary figure 1a. Instead, the incorporation of fibres in the resins results in
399 chipping and fracture of fibres instead of polymeric fractures, and the composite's ability to
400 withstand repetitive impact loads is greatly enhanced. The degree of surface cracks can be
401 greatly reduced on the coating surface after the incorporation of fibres. Fibres also hold the
402 polymeric structure in place and provide a discontinuous path for shock transmission through
403 the material as compared to the pure polymeric resin, as simulated in figure 7c.

404 To conclude, the fibre structures in elastomeric coatings effectively distribute the water
405 droplets/sands energy across the composite structures without significant damage to the
406 polyurethane matrix. The inclusion of fibres is also known to prevent crack initiations,
407 making them the ideal candidate for icephobic applications, particularly since cracks serve as
408 possible ice anchoring points. Specifically, carbon fibre reinforced coatings are promising
409 candidates for icephobic applications as they have superior fatigue resistance as compared to
410 Kevlar fibre filled composites [48]. Our experiments confirmed that the carbon fibre
411 reinforced coatings had better erosion resistance and the surface cavities were much smaller
412 on Kevlar fibre-reinforced coatings. Carbon fibre reinforced elastomeric coatings have all
413 four characteristics for ideal durable icephobic coatings: higher erosion resistance, inhibition
414 of surface cracks, ability to resist the plastic deformation, and stiff fibres to withstand against
415 the significant structural loading conditions.

416 **4 Conclusions**

417 A new approach was developed to enhance the durability of low ice adhesion polyurethane
418 coatings in this study. The incorporation of micro-fibres and nanoparticles in the coating
419 matrix was driven by the need of enhancing durability in surface icephobicity under erosion
420 impact. Ice adhesion strength after erosion was maintained to a low level with the
421 incorporation of the fillers as compared to the pure PU coatings.

422 It was found that the fibre reinforcement was more effective in restricting the surface damage
423 as compared to the addition of nanofillers. The ice adhesion strengths on the pristine and
424 impinged PU coatings were 2.6 kPa and 83.1 kPa, respectively. As a comparison, the ice
425 adhesion strength of the PU coatings with 20 wt% carbon fibres slightly increased from 5.6
426 kPa to 8.4 kPa, essentially keeping the adhesion below 10 kPa even after the erosion, and a
427 ~10-fold reduction in ice adhesion strength was achieved as compared to that of the pure PU
428 coatings. This distinction could be explained by better interfacial bonding and higher aspect
429 ratio of the carbon fibres in the PU matrix.

430 The significantly improved icephobic durability of the carbon fibre-reinforced PU coatings
431 could be attributed to the reduced number and shallowed surface cavities. The number/size of
432 surface cavities formed during water erosion, which could act as possible ice anchoring
433 points, were minimized with the incorporation of the fillers. The inclusion of fibres helps to
434 distribute the droplet/sand impact energy more widely which could reduce the stress
435 concentration in the coatings by minimizing crack initiation during the incubation period. The
436 methodology proposed in this work can also be used for the durability enhancement of other
437 polymeric coatings, especially the coatings designed for high-impingement conditions or
438 erosive environments.

439 **Acknowledgements**

440 This work was supported by a studentship from the Faculty of Engineering, University of
441 Nottingham and was partially funded by the CleanSky 2 Joint Undertaking under the
442 European Union’s Horizon 2020 research and innovation programme under grant agreement
443 No CS2-AIR-GAM-2014-2015-O1. Cf. Art.29.4 of [A2]. The authors also thank Dr. Barbara
444 Turnbull for helping with ice adhesion strength tests and acknowledge the use of facilities at
445 the Nanoscale and Microscale Research Centre of the University of Nottingham supported by
446 Engineering and Physical Sciences Research Council [grant number EP/L022494/1]. The
447 authors are grateful to Teijin Aramid GmbH, Germany, for kindly supplying Twaron Kevlar
448 fibres pulp.

449 **References**

- 450 [1] T. Mahmut, H. Memon, F. Xu, I. Ahmed, X. Hou, Electrospun nanofibre membrane based
451 transparent slippery liquid-infused porous surfaces with icephobic properties, *Colloids and*
452 *Surfaces A: Physicochemical and Engineering Aspects* 585 (2020) 124177.
453
- 454 [2] W. Cui, T.A. Pakkanen, Fabrication of transparent icephobic surfaces with self-
455 reparability: Effect of structuring and thickness of the lubricant-elastomer layer, *Applied*
456 *Surface Science* 504 (2020) 144061.
457
- 458 [3] K. Golovin, A. Dhyani, M. Thouless, A. Tuteja, Low–interfacial toughness materials for
459 effective large-scale deicing, *Science* 364(6438) (2019) 371-375.
460
- 461 [4] J. Liu, J. Wang, H. Memon, Y. Fu, T. Barman, K.-S. Choi, X. Hou,
462 Hydrophobic/icephobic coatings based on thermal sprayed metallic layers with subsequent
463 surface functionalization, *Surface and Coatings Technology* 357 (2019) 267-272.
464
- 465 [5] E. Vazirinasab, K. Maghsoudi, R. Jafari, G. Momen, A comparative study of the
466 icephobic and self-cleaning properties of Teflon materials having different surface
467 morphologies, *Journal of Materials Processing Technology* 276 (2020) 116415.
468
- 469 [6] R.K. Moghadam, M.T. Rahni, K. Javadi, S.H. Davoudian, R. Miller, Influence of New
470 Superhydrophobic Micro-structures on Delaying Ice Formation, *Colloids and Surfaces A:*
471 *Physicochemical and Engineering Aspects* (2020) 124675.
472
- 473 [7] F. Piscitelli, A. Chiariello, D. Dabkowski, G. Corrado, F. Marra, L.D. Palma,
474 Superhydrophobic Coatings as Anti-Icing Systems for Small Aircraft, *Aerospace* 7(1) (2020)
475 2.
476
- 477 [8] Y. Shen, Y. Wu, J. Tao, C. Zhu, H. Chen, Z. Wu, Y. Xie, Spraying fabrication of durable
478 and transparent coatings for anti-icing application: dynamic water repellency, icing delay,
479 and ice adhesion, *ACS applied materials & interfaces* 11(3) (2018) 3590-3598.
480
- 481 [9] Z.A. Janjua, B. Turnbull, K.-L. Choy, C. Pandis, J. Liu, X. Hou, K.-S. Choi, Performance
482 and durability tests of smart icephobic coatings to reduce ice adhesion, *Applied Surface*
483 *Science* 407 (2017) 555-564.
484
- 485 [10] J.H. Kim, M.J. Kim, B. Lee, J.M. Chun, V. Patil, Y.-S. Kim, Durable ice-lubricating
486 surfaces based on polydimethylsiloxane embedded silicone oil infused silica aerogel, *Applied*
487 *Surface Science* (2020) 145728.
488
- 489 [11] D. Wu, L. Ma, F. Zhang, H. Qian, B. Minhas, Y. Yang, X. Han, D. Zhang, Durable
490 deicing lubricant-infused surface with photothermally switchable hydrophobic/slippy
491 property, *Materials & Design* 185 (2020) 108236.
492
- 493 [12] J. Wang, H. Memon, J. Liu, G. Yang, F. Xu, T. Hussain, C. Scotchford, X. Hou, Effect
494 of surface adsorption on icing behaviour of metallic coating, *Surface and Coatings*
495 *Technology* 380 (2019) 125068.

- 496 [13] K. Golovin, S.P. Kobaku, D.H. Lee, E.T. DiLoreto, J.M. Mabry, A. Tuteja, Designing
497 durable icephobic surfaces, *Science advances* 2(3) (2016) e1501496.
498
- 499 [14] W. Tong, D. Xiong, N. Wang, Z. Wu, H. Zhou, Mechanically robust superhydrophobic
500 coating for aeronautical composite against ice accretion and ice adhesion, *Composites Part B:
501 Engineering* 176 (2019) 107267.
502
- 503 [15] Y. Zhuo, S. Xiao, V. Håkonsen, T. Li, F. Wang, J. He, Z. Zhang, Ultrafast self-healing
504 and highly transparent coating with mechanically durable icephobicity, *Applied Materials
505 Today* 19 (2020) 100542.
506
- 507 [16] X. Wu, X. Zhao, J.W.C. Ho, Z. Chen, Design and durability study of environmental-
508 friendly room-temperature processable icephobic coatings, *Chemical Engineering Journal*
509 355 (2019) 901-909.
510
- 511 [17] Y.H. Yeong, A. Millionis, E. Loth, J. Sokhey, Self-lubricating icephobic elastomer
512 coating (SLIC) for ultralow ice adhesion with enhanced durability, *Cold Regions Science and
513 Technology* 148 (2018) 29-37.
514
- 515 [18] F. Wang, W. Ding, J. He, Z. Zhang, Phase transition enabled durable anti-icing surfaces
516 and its DIY design, *Chemical Engineering Journal* 360 (2019) 243-249.
517
- 518 [19] X. Wu, Z. Chen, A mechanically robust transparent coating for anti-icing and self-
519 cleaning applications, *Journal of Materials Chemistry A* 6(33) (2018) 16043-16052.
520
- 521 [20] D.L. Beemer, W. Wang, A.K. Kota, Durable gels with ultra-low adhesion to ice, *Journal
522 of Materials Chemistry A* 4(47) (2016) 18253-18258.
523
- 524 [21] Y. Zhuo, T. Li, F. Wang, V. Håkonsen, S. Xiao, J. He, Z. Zhang, An ultra-durable
525 icephobic coating by a molecular pulley, *Soft Matter* 15(17) (2019) 3607-3611.
526
- 527 [22] J. Liu, J. Wang, L. Mazzola, H. Memon, T. Barman, B. Turnbull, G. Mingione, K.-S.
528 Choi, X. Hou, Development and evaluation of poly (dimethylsiloxane) based composite
529 coatings for icephobic applications, *Surface and Coatings Technology* 349 (2018) 980-985.
530
- 531 [23] H. Memon, J. Liu, N. Weston, J. Wang, D.S. De Focatiis, K.-s. Choi, X. Hou, In-situ
532 icing and water condensation study on different topographical surfaces, *Cold Regions
533 Science and Technology* 165 (2019) 102814.
534
- 535 [24] H. Memon, J. Liu, D.S. De Focatiis, K.-s. Choi, X. Hou, Intrinsic dependence of ice
536 adhesion strength on surface roughness, *Surface and Coatings Technology* 385 (2020)
537 125382.
538
- 539 [25] S. Kulinich, M. Farzaneh, Ice adhesion on super-hydrophobic surfaces, *Applied Surface
540 Science* 255(18) (2009) 8153-8157.
541
- 542 [26] C. Laforte, A. Beisswenger, Icephobic material centrifuge adhesion test, *Proceedings of
543 the 11th International Workshop on Atmospheric Icing of Structures, IWAIS, Montreal, QC,
544 Canada, 2005, pp. 12-16.*
545

- 546 [27] C. Laforte, C. Blackburn, J. Perron, and R. Aubert, Icephobic coating evaluation for
547 aerospace application. In 55th AIAA/ASME/ASCE/AHS/SC Structures, Structural Dynamics,
548 and Materials Conference, 2014, pp. 1327.
549
- 550 [28] S. Rønneberg, Y. Zhuo, C. Laforte, J. He and Z. Zhang, Interlaboratory study of ice
551 adhesion using different techniques, *Coatings* 9(10) (2019) 678.
552
- 553 [29] J.D. Pampush, D.J. Daegling, A.E. Vick, W.S. McGraw, R.M. Covey and A.J. Rapoff
554 Technical note: Converting durometer data into elastic modulus in biological materials, *Am.*
555 *J. Phys. Anthropol* 146 (2011) 650-653.
556
- 557 [30] I.M. Meththananda, S. Parker, M.P. Patel and M. Braden, The relationship between
558 Shore hardness of elastomeric dental materials and Young's modulus, *Dental materials*, 25(8)
559 (2009) 956-959.
560
- 561 [31] C. Wang, T. Fuller, W. Zhang, K.J. Wynne, Thickness dependence of ice removal stress
562 for a polydimethylsiloxane nanocomposite: Sylgard 184, *Langmuir* 30(43) (2014) 12819-
563 12826.
564
- 565 [32] I. Neitzel, V. Mochalin, I. Knoke, G.R. Palmese, Y. Gogotsi, Mechanical properties of
566 epoxy composites with high contents of nanodiamond, *Composites science and technology*
567 71(5) (2011) 710-716.
568
- 569 [33] V.N. Mochalin, Y. Gogotsi, Nanodiamond–polymer composites, *Diamond and Related*
570 *Materials* 58 (2015) 161-171.
571
- 572 [34] S. Roy, K. Mitra, C. Desai, R. Petrova, S. Mitra, Detonation nanodiamonds and carbon
573 nanotubes as reinforcements in epoxy composites—a comparative study, *Journal of*
574 *Nanotechnology in Engineering and Medicine* 4(1) (2013).
575
- 576 [35] D. Cai, K. Yusoh, M. Song, The mechanical properties and morphology of a graphite
577 oxide nanoplatelet/polyurethane composite, *Nanotechnology* 20(8) (2009) 085712.
578
- 579 [36] B. Fiedler, F.H. Gojny, M.H.G. Wichmann, M.C.M. Nolte, K. Schulte, Fundamental
580 aspects of nano-reinforced composites, *Composites Science and Technology* 66(16) (2006)
581 3115-3125.
582
- 583 [37] R.E. Lavengood, L.B. Gulbransen, The effect of aspect ratio on the fatigue life of short
584 boron fiber reinforced composites, *Polymer Engineering & Science* 9(5) (1969) 365-369.
585
- 586 [38] O.G. Engel, Erosion damage to solids caused by high speed collision with rain, *Journal*
587 *of Research of the National Bureau of Standards* 61(1) (1958) 47-52.
588
- 589 [39] O. Gohardani, Impact of erosion testing aspects on current and future flight conditions,
590 *Progress in Aerospace Sciences* 47(4) (2011) 280-303.
591
- 592 [40] J.H. Brunton, F.P. Bowden, A discussion on deformation of solids by the impact of
593 liquids, and its relation to rain damage in aircraft and missiles, to blade erosion in steam
594 turbines, and to cavitation erosion - High speed liquid impact, *Philosophical Transactions of*

595 the Royal Society of London. Series A, Mathematical and Physical Sciences 260(1110)
596 (1966) 79-85.
597
598 [41] D. Eisenberg, S. Laustsen, J. Stege, Wind turbine blade coating leading edge rain erosion
599 model: Development and validation, *Wind Energy* 21(10) (2018) 942-951.
600
601 [42] H. Slot, E. Gelinck, C. Rentrop, E. Van Der Heide, Leading edge erosion of coated wind
602 turbine blades: Review of coating life models, *Renewable Energy* 80 (2015) 837-848.
603
604 [43] B. Amirzadeh, A. Louhghalam, M. Raessi, M. Tootkaboni, A computational framework
605 for the analysis of rain-induced erosion in wind turbine blades, part II: Drop impact-induced
606 stresses and blade coating fatigue life, *Journal of Wind Engineering and Industrial
607 Aerodynamics* 163 (2017) 44-54.
608
609 [44] M. Elhadi Ibrahim, M. Medraj, Water Droplet Erosion of Wind Turbine Blades:
610 Mechanics, Testing, Modeling and Future Perspectives, *Materials* 13(1) (2020) 157.
611
612 [45] M. Mahdipoor, H. Kirols, D. Kevorkov, P. Jedrzejowski, M. Medraj, Influence of impact
613 speed on water droplet erosion of TiAl compared with Ti6Al4V, *Scientific reports* 5 (2015)
614 14182.
615
616 [46] W. Adler, The mechanics of liquid impact, Academic Press, *Treatise on Materials
617 Science and Technology* 16 (1979) 127-183.
618
619 [47] W. Adler, R. Vyhnal, Rain erosion of Ti-6Al-4V, *Proceedings, AA Fyall and RB King,*
620 *eds* 2 (1974) 539-569.
621
622 [48] J.D. Buckley, D.D. Edie, *Carbon-carbon materials and composites*, William Andrew,
623 1993.

624 **List of Figures**

- 625 1. (a) Ice formation on a sample surface and (b) the details of the centrifugal testing method
626 (figure created using biorender.com)
- 627 2. Effect of fillers on the Shore D hardness of polymer coatings
- 628 3. Microstructural images of (a) before and (b) after WIETs on the pure PU coatings and
629 after WIETs on (c) PU-ND-3, (b) PU-ND-20, (e) PU-KV-3, and (f) PU-KV-20 coatings
- 630 4. (a) 3D profile and (b) 2D image of PU-ND-40 coatings and (c) 3D profile and (d) 2D
631 image of PU-KV-20 coatings after WIETs
- 632 5. (a) PU-KV-20 and (b) PU-CF-20 coatings after WIETs. Possible material damage around
633 the incorporated (c) Kevlar and (d) carbon fibres
- 634 6. Ice adhesion strength in comparison to (a) Shore D hardness values, surface roughness (b)
635 before and (c) after WIETs. (d) Ice adhesion strength before and after WIETs
- 636 7. (a) Stress waves generated after the impact of a water droplet/sand particles (The
637 mechanism is adapted from [39]) and the stress waves on (b) a pristine polymer and (c) a
638 fibre-reinforced polymer (figure created using biorender.com)

639